


# Thermal transport properties of 2D narrow bandgap semiconductor $Ca_3N_2$, $Ba_3P_2$, and $Ba_3As_2$: Machine learning potential study

Wenlong Li(李文龙), Yu Liu(刘余), Zhendong Li(李振东), Pei Zhang(张培), Xinghua Li(李兴华), and Tao Ouyang(欧阳滔)

**Citatio:**Chin. Phys. B, 2025, 34 (**9**): 096302. DOI: 10.1088/1674-1056/ade5a0
http://cpb.iphy.ac.cn; http://iopscience.iop.org/cpb

**What follows is a list of articles you may be interested in**

---

## Lattice and phonon properties in semiconductors $FeSb_2$ and $RuSb_2$

Meng Zhang(张萌), Shengnan Dai(戴胜男), Ranran Zhang(张冉冉), Mingfang Shu(舒明方), Wei Xu(徐威), Jinfeng Zhu(朱金峰), Xianglin Liu(刘祥麟), Yixuan Luo(罗伊轩), Toru Ishigaki, Bo Duan(段波), Yanfeng Guo(郭艳峰), Zhe Qu(屈哲), Jiong Yang(杨炯), and Jie Ma(马杰)

Chin. Phys. B, 2025, 34 (**8**): 086302. DOI: 10.1088/1674-1056/adda0e

## Dynamic response of a thermal transistor to time-varying signals

Qinli Ruan(阮琴丽), Wenjun Liu(刘文君), and Lei Wang(王雷)

Chin. Phys. B, 2024, 33 (**5**): 056301. DOI: 10.1088/1674-1056/ad2dcc

## Impeded thermal transport in aperiodic BN/C nanotube superlattices due to phonon Anderson localization

Luyi Sun(孙路易), Fangyuan Zhai(翟方园), Zengqiang Cao(曹增强), Xiaoyu Huang(黄晓宇), Chunsheng Guo(郭春生), Hongyan Wang(王红艳), and Yuxiang Ni(倪宇翔)

Chin. Phys. B, 2023, 32 (**5**): 056301. DOI: 10.1088/1674-1056/acb9e7

## Prediction of lattice thermal conductivity with two-stage interpretable machine learning

Jinlong Hu(胡锦龙), Yuting Zuo(左钰婷), Yuzhou Hao(郝昱州), Guoyu Shu(舒国钰), Yang Wang(王洋), Minxuan Feng(冯敏轩), Xuejie Li(李雪洁), Xiaoying Wang(王晓莹), Jun Sun(孙军), Xiangdong Ding(丁向东), Zhibin Gao(高志斌), Guimei Zhu(朱桂妹), and Baowen Li(李保文)

Chin. Phys. B, 2023, 32 (**4**): 046301. DOI: 10.1088/1674-1056/acbaf4

## Lattice thermal conduction in cadmium arsenide

R F Chinnappagoudra, M D Kamatagi, N R Patil, and N S Sankeshwar

Chin. Phys. B, 2022, 31 (**11**): 116301. DOI: 10.1088/1674-1056/ac7863

---

**SPECIAL TOPIC — Heat conduction and its related interdisciplinary areas**

# Thermal transport properties of 2D narrow bandgap semiconductor $Ca_3N_2$, $Ba_3P_2$, and $Ba_3As_2$: Machine learning potential study

Wenlong Li(李文龙)[1,†], Yu Liu(刘余)[1,†], Zhendong Li(李振东)[1], Pei Zhang(张培)[2,‡], Xinghua Li(李兴华)[3,§], and Tao Ouyang(欧阳滔)[1]

[1] *School of Physics and Optoelectronics, Xiangtan University, Xiangtan* 411105, *China*

[2] *Hunan Provincial Key Laboratory of Intelligent Sensors and Advanced Sensor Materials, School of Physics and Electronics, Hunan University of Science and Technology, Xiangtan* 411201, *China*

[3] *Hunan International Intellectual Exchange and Cooperation Center, Changsha* 410013, *China*

(Received 8 May 2025; revised manuscript received 5 June 2025; accepted manuscript online 18 June 2025)

By combining neuroevolution potential (NEP) with phonon Boltzmann transport theory, we systematically investigate the thermal transport properties of three two-dimensional (2D) narrow bandgap semiconductors: $Ca_3N_2$, $Ba_3P_2$, and $Ba_3As_2$. The room-temperature lattice thermal conductivities ($\kappa_L$) of $Ca_3N_2$, $Ba_3P_2$, and $Ba_3As_2$ considering only three-phonon scattering are 6.60 W/mK, 11.90 W/mK, and 8.88 W/mK, respectively. When taking into account the higher-order phonon (four-phonon) scattering processes, the $\kappa_L$ of these three materials decrease to 6.12 W/mK, 9.73 W/mK and 6.77 W/mK, respectively. Among these systems, $Ba_3As_2$ undergoes the most pronounced suppression with a reduction of 23.8%. This is mainly due to the greater scattering phase space which enhances the four-phonon scattering. Meanwhile, it is revealed that unlike the traditional evaluation using the $P_4/P_3$ ratio as an indicator of the strength of four-phonon interactions, the thermal conductivity of $Ba_3P_2$ exhibits weaker four-phonon suppression behavior compared to $Ba_3As_2$, despite hosting a higher $P_4/P_3$ ratio. That is to say, the strength of four-phonon scattering cannot be evaluated solely by the ratio of $P_4/P_3$. These results presented in this work shed light on the thermal transport properties of such new 2D semiconductors with narrow bandgaps.

**Keywords:** narrow-bandgap semiconductor materials, neuroevolution potential (NEP), four-phonon (4ph) scattering, lattice thermal conductivity ($\kappa_L$)

**PACS:** 63.20.–e, 63.20.Ry, 66.70.Df, 02.70.–c

**DOI:** 10.1088/1674-1056/ade5a0 **CSTR:** 32038.14.CPB.ade5a0

## 1. Introduction

In recent years, two-dimensional (2D) materials have gained extensive attention in condensed matter physics and materials science due to their unique electronic structures and exceptional thermal transport properties.[1–6] Since the successful mechanical exfoliation of graphene, emerging 2D material systems, including hexagonal boron nitride (h-BN),[7,8] black phosphorus,[9,10] and transition metal dichalcogenides (TMDCs),[11,12] have demonstrated tremendous potential for nanoscale thermal management applications. Within the realm of two-dimensional functional materials, narrow-bandgap semiconductors exhibit distinctive electron–phonon coupling effects and tunable thermoelectric transport characteristics. Compared with conventional wide-bandgap semiconductors, narrow-bandgap materials demonstrate remarkable intrinsic carrier excitation behavior near room temperature. Meanwhile, the thermal conductivity of narrow-bandgap materials is highly responsive to changes in temperature, mechanical strain, and dimensional scaling, thereby offering diverse physical avenues for modulating the thermal transport behavior of narrow-bandgap semiconductors. Recent systematic investigations by the research group of Chen *et al.*[13] on $Ca_3N_2$, $Ba_3P_2$, and $Ba_3As_2$ have revealed their distinctive characteristics, including intrinsic narrow bandgaps, remarkable electrical conductivity, and excellent energetic stability. For instance, $Ba_3As_2$ exhibits an electron mobility as high as $1.37 \times 10^4$ $cm^2 \cdot V^{-1} \cdot s^{-1}$ along the $x$-direction, highlighting its potential for high-performance electronic applications. In terms of stability, the cohesive energies of $Ca_3N_2$, $Ba_3P_2$, and $Ba_3As_2$ are calculated to be 3.89 eV/atom, 3.39 eV/atom, and 3.24 eV/atom, respectively, indicating strong structural robustness. These excellent properties emphasize the importance of deeply investigating their heat transport properties to assess their potential as next-generation, highly efficient semiconductor materials.

Combination of the density functional theory (DFT) simulations and phonon Boltzmann transport equation (PBTE) represents one of the most reliable approaches for evaluating the thermal conductivity of materials. However, incorporating

[†]These authors contributed equally to this work.

[‡]Corresponding author. E-mail: zhangpei@hnust.edu.cn

[§]Corresponding author. E-mail: xinghualee@139.com

© 2025 Chinese Physical Society and IOP Publishing Ltd. All rights, including for text and data mining, AI training, and similar technologies, are reserved.

four-phonon (4ph) scattering effects requires computationally intensive calculations of anharmonic third- and fourth-order force constants, often involving thousands of single-point energy evaluations, resulting in prohibitive resource and time costs. In recent years, the emergence of machine learning potentials (MLPs),[14,15] including Gaussian approximation potentials (GAP),[16,17] atomic cluster expansion (ACE),[18,19] deep learning potential (DP),[20,21] moment tensor potential (MTP),[22,23] and neuroevolution potential (NEP),[24] has significantly reduced such computational overhead while improving computational efficiency. Among these MLPs, NEP stands out in thermal transport studies due to its exceptional accuracy, transferability, and computational efficiency.[25,26] NEP is obtained by fitting a first-principles dataset, which predicts force constants with the accuracy of DFT. Tang *et al.*[27] successfully employed NEP to study lattice dynamics and phonon thermal transport in cubic $ScF_3$. Zhang *et al.*[28] used NEP to study the thermal conductivity of GeTe, and the calculated results are consistent with experimental data and those obtained from the Boltzmann transport method. These cases provide strong evidence of the reliability of NEP models for thermal transport studies.

Motivated by the above statements, combining the typical MLP of NEP with phonon Boltzmann transport theory (PBTE), the thermal transport in 2D semiconductors with narrow bandgaps, namely $Ca_3N_2$, $Ba_3P_2$, and $Ba_3As_2$, is systematically investigated. The results reveal that the three materials all have low thermal conductivities: only three-phonon scattering considered are 6.60 W/mK, 11.90 W/mK, and 8.88 W/mK, respectively. When taking into account the fourth-order phonon scattering processes, the thermal conductivities are 6.12 W/mK, 9.73 W/mK, and 6.77 W/mK, respectively. The most pronounced suppression among these systems occurs in $Ba_3As_2$, with a reduction of 23.8%, primarily due to the enhanced four-phonon scattering caused by a greater scattering phase space. This study reveals that, contrary to the conventional use of the $P_4/P_3$ ratio as an indicator of four-phonon interaction strength, the thermal conductivity of $Ba_3P_2$ exhibits weaker four-phonon suppression compared to $Ba_3As_2$, despite having a higher $P_4/P_3$ ratio. Thus, the strength of four-phonon scattering cannot be assessed solely by the $P_4/P_3$ ratio. These findings provide new insights into the thermal transport properties of novel 2D semiconductors with narrow bandgaps.

## 2. Computational methods

In this work, the first-principles calculations are implemented in the Vienna *Ab initio* simulation package (VASP).[29] We use the projector-augmented wave (PAW) method[30,31] for the ion–electron interactions, and the Perdew–Burke–Ernzerhof (PBE) functional within the generalized gradient approximation (GGA) is employed as the exchange–correlation potential.[32] The wave functions are expanded in a plane-wave basis with a kinetic energy cutoff of 500 eV, and a $k$-mesh of $9\times9\times1$ is used to sample the Brillouin zone. Structural relaxations are performed with convergence criteria of $10^{-8}$ eV and $10^{-4}$ eV/Å for energy and forces, respectively. A large vacuum region of 30 Å is set to avoid the interactions between the monolayer and its periodic images induced by the boundary conditions. For the thermal conductivity calculations, we accurately describe the phonon transport behavior by rigorously solving the phonon Boltzmann transport equation. Within the framework of PBTE, the $\kappa_{\rm L}$ of the system can be expressed as[33]

$$\kappa_{\rm L}^{\alpha\beta}=\frac{1}{k_{\rm B}T^2VN}\sum_{\lambda}f_{\lambda}^{0}(f_{\lambda}^{0}+1)\,(\hbar w_{\lambda})^2V_{\lambda}^{\alpha}F_{\lambda}^{\beta}. \tag{1}$$

Here, $k_{\rm B}$ is the Boltzmann constant, $T$ is the temperature, $V$ is the volume of the unit cell, and $N$ is the number of $q$-points uniformly distributed in the discretized first Brillouin zone. $f_{\lambda}^{0}$ is the phonon occupation number for a given phonon mode $\lambda$ based on Bose–Einstein statistics. $\hbar$ is the reduced Planck constant, $w_{\lambda}$ is the phonon frequency, and $V_{\lambda}^{\alpha}$ is the phonon group velocity in the $\alpha$ direction. The finite difference method enables the determination of interatomic force constants (IFCs) of each order within the supercell. Notably, fourth-order force constants are sensitive to the choice of the step size in the calculation process.[34] We therefore set the displacement used for fourth-order calculations to 0.04 Å to ensure robust energy convergence. The software used for calculating the 2nd-, 3rd-, and 4th-order IFCs are PHONOPY,[35] thirdorder_vasp.py,[36] and Fourthorder_vasp.py,[37] respectively. The size of the supercell is $9\times9\times1$. The cutoff distance for the 3rd-order IFCs is set to the sixth nearest-neighbor atoms, while the cutoff for the 4th-order IFCs is the third nearest-neighbor atoms. We solve the BTE iteratively for three-phonon (3ph) scattering processes and use the relaxation time approximation for four-phonon (4ph) scattering processes. Maximum likelihood estimation is employed to estimate scattering rates from a limited sample of scattering processes. The sample size for four-phonon interactions is set to 400000, which, according to Guo *et al.*,[38] is sufficient to ensure computational accuracy while enhancing computational efficiency. Taking $Ca_3N_2$ as an example, the convergence of $\kappa_{\rm L}$ is rigorously analyzed and the results are provided as follows. To balance computation cost and accuracy, a phonon $N$-grid of $51\times51\times1$ and a scale-broad of 1.0 are used to compute the convergent three- and four-phonon information.

The NEP is initially trained using a dataset derived from *ab initio* molecular dynamics (AIMD) calculations, with the work performed utilizing the NEP code, as implemented in the GPUMD package.[26] Static self-consistent calculations are conducted for these configurations, and basic information such as atomic forces and energies is extracted into the training set to obtain the energy, force, and virial data for NEP

training. The Nose–Hoover method as implemented in the VASP package is used for temperature control in the AIMD simulation at 300 K with the canonical ensemble (NVT). We rigorously test each component separately to quantify their individual impacts. We then employ 100 configurations from AIMD. A $5 \times 5 \times 1$ supercell (with 125 atoms) is subjected to a 3% random box deformation and a 0.1 Å random displacement of each atom, producing 200 structures and resulting in a total of 300 configurations for each structure. The radial ($r_c^R$) and angular ($r_c^A$) cutoff settings play a decisive role in the NEP model's precision. $r_c^R = 8$ Å and $r_c^A = 4$ Å are selected after the individual impacts of each component are quantified through rigorous isolated testing.

## 3. Results and discussion

Figure 1 displays the top- and side-view crystal structures of $Ca_3N_2$, $Ba_3P_2$, and $Ba_3As_2$, which all belong to the *P*-3*m*1 space group (No. 164). As presented in Table 1, the lattice vectors $\boldsymbol{a}$ and $\boldsymbol{b}$ are equal, and the corresponding lattice angles are $\alpha = \beta = 90^\circ$ and $\gamma = 120^\circ$. The calculations are in good agreement with previously reported data,[13] confirming the reliability of our computation. Owing to the high degree of hexagonal symmetry, these three 2D materials are expected to exhibit enhanced structural stability. As evidenced by previous research, all three 2D materials exhibit outstanding thermal stability combined with ultrahigh ideal strength and superior ductility over the range from ambient to high temperatures (300–600 K). This remarkable stability endows these three 2D materials with broad application prospects.

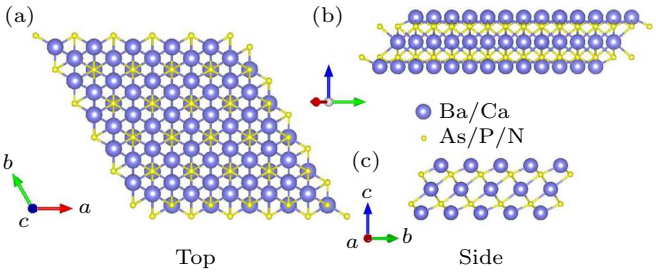



**Fig. 1.** Top and side views of the monolayer structures of $Ca_3N_2$, $Ba_3P_2$, and $Ba_3As_2$.

**Table 1.** Calculated lattice parameters in this work (previous study[13] data are noted by *), total three-phonon scattering phase space ($P_3$), total four-phonon scattering phase space ($P_4$), square of the total Grüneisen parameter (total $\gamma^2$) (300 K) of $Ca_3N_2$, $Ba_3P_2$, and $Ba_3As_2$.

| Structure | $Ca_3N_2$ | $Ba_3P_2$ | $Ba_3As_2$ |
|---|---|---|---|
| $a = b$ (Å) | 3.665(3.691*) | 4.782(4.811*) | 4.955(4.955*) |
| $a = b$ (Å) (without vdW) | 3.665 | 4.782 | 4.953 |
| $\alpha = \beta$ (°) | 90 | 90 | 90 |
| $\gamma$ (°) | 120 | 120 | 120 |
| Total $P_3$ | $1.226 \times 10^{-2}$ | $8.371 \times 10^{-3}$ | $1.278 \times 10^{-2}$ |
| Total $P_4$ | $9.108 \times 10^{-3}$ | $8.700 \times 10^{-3}$ | $1.119 \times 10^{-2}$ |
| Total $\gamma^2$ (300 K) | 2.769 | 2.614 | 1.778 |

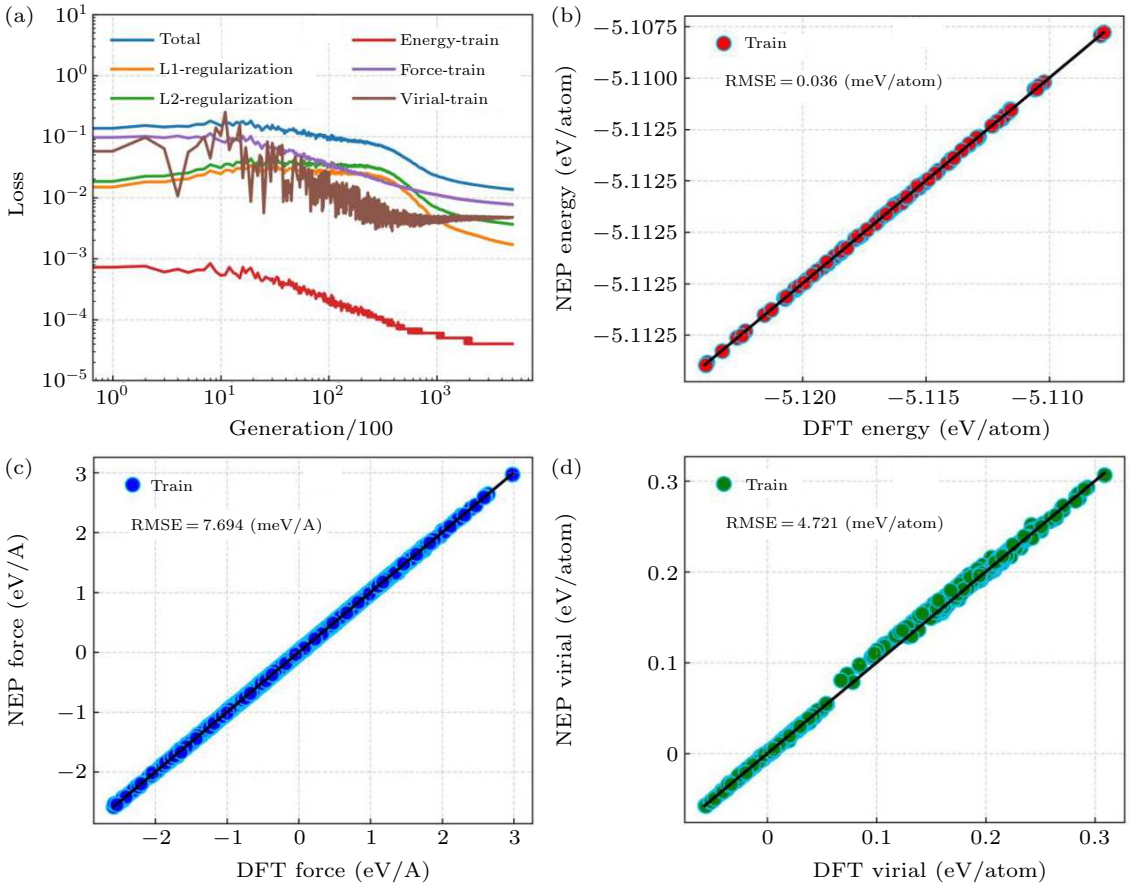



**Fig. 2.** (a) Evolution of the loss functions (total, L1, L2, energy, force, and virial) during the training process. (b)–(d) Comparison of NEP-calculated (b) forces, (c) energies, and (d) virials with DFT reference data for the initial training dataset of $Ca_3N_2$.

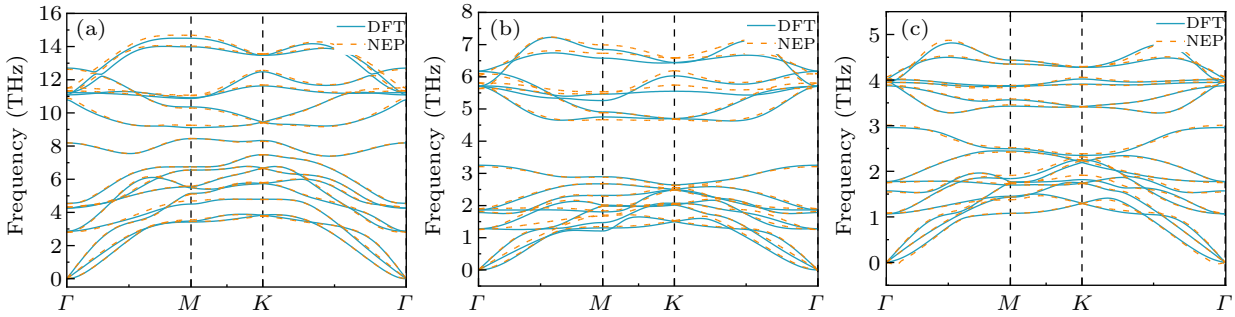



**Fig. 3.** Phonon dispersion of (a) $Ca_3N_2$, (b) $Ba_3P_2$, and (c) $Ba_3As_2$ calculated based on DFT and NEP.

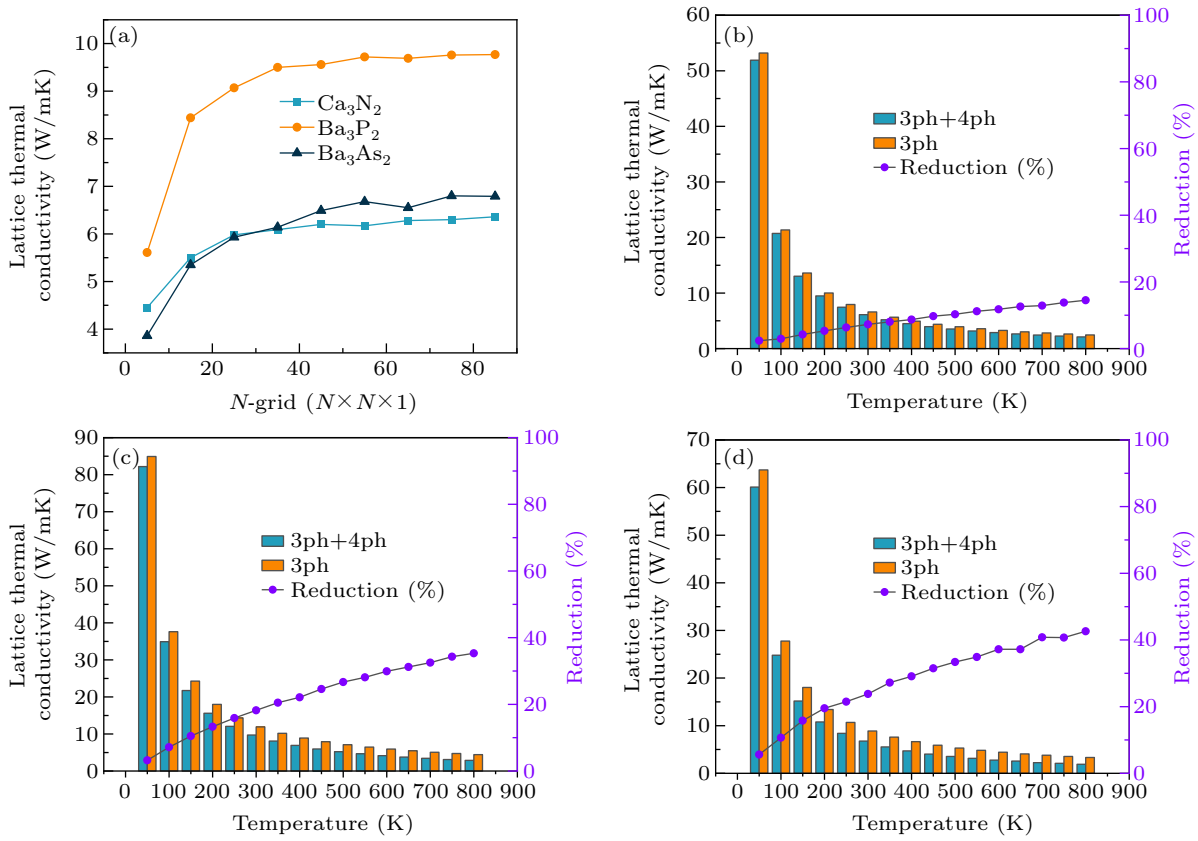



**Fig. 4.** (a) Thermal conductivity convergence test (considering three- and four-phonon scattering processes) of $Ca_3N_2$, $Ba_3P_2$, and $Ba_3As_2$. (b)–(d) The values of $\kappa_{3ph}$ and $\kappa_{3ph+4ph}$ at different temperatures, and the percentage reduction in $\kappa_L$ due to 4ph scattering for (b) $Ca_3N_2$, (c) $Ba_3P_2$, and (d) $Ba_3As_2$.

As illustrated in Fig. 2 for $Ca_3N_2$ (corresponding figures for $Ba_3P_2$ and $Ba_3As_2$ are provided as Figs. S1 and S2 in the supplemental material), the small root-mean-square errors (RMSEs) for both single-atom energies and atomic forces across these compounds highlight the computational accuracy of NEP (0.036 meV/atom, 0.020 meV/atom, and 0.041 meV/atom for $Ca_3N_2$, $Ba_3P_2$, and $Ba_3As_2$, respectively), which is comparable to DFT results. Moreover, the phonon dispersion obtained from the NEP-based calculation is highly consistent with that obtained from the DFT calculations (shown in Fig. 3). This consistency in phonon dispersion and atomic-level interactions ensures the reliability of subsequent thermal transport property calculations.

In Fig. 4(a), we depict the thermal conductivity as a function of the phonon $N$-grid for these three 2D materials (considering both three- and four-phonon scattering processes). To ensure conciseness, only the plots including three- and four-phonon scattering processes are shown in the main text, while those considering only three-phonon scattering are provided in the supplemental material. It is evident that as the phonon $N$-grid increases, the thermal conductivity approaches a stable value, ensuring that converged phonon transport information is obtained. Figures 4(b)–4(d) illustrate the lattice thermal conductivity of $Ca_3N_2$, $Ba_3P_2$, and $Ba_3As_2$ considering three-phonon scattering processes (denoted as $\kappa_{3ph}$) and four-phonon scattering processes (denoted as $\kappa_{3ph+4ph}$). Clearly, with increasing temperature, the thermal conductivity decreases, consistent with the expected temperature-dependent relationship, indicating that the thermal conductivity is predominantly governed by anharmonic phonon–phonon interac-

tions. The $\kappa_{3ph}$ of $Ca_3N_2$, $Ba_3P_2$, and $Ba_3As_2$ at 300 K were calculated as 6.60 W/mK, 11.90 W/mK, and 8.88 W/mK, respectively, whereas the corresponding $\kappa_{3ph+4ph}$ values were 6.12 W/mK, 9.73 W/mK, and 6.77 W/mK. $\kappa_{3ph+4ph}$ exhibits reductions of 7.3%, 18.2%, and 23.8% relative to $\kappa_{3ph}$. Notably, the suppression effect of four-phonon scattering on $\kappa_L$ is enhanced with increasing temperature; for example, in $Ba_3P_2$, the reduction increases from 7.2% at 100 K to 35.3% at 800 K, whereas $Ba_3As_2$ shows an even more pronounced trend, rising from 10.7% to 42.6% over the same temperature range. These results clearly demonstrate that the four-phonon effect is not negligible in these materials, particularly in the high-temperature region.

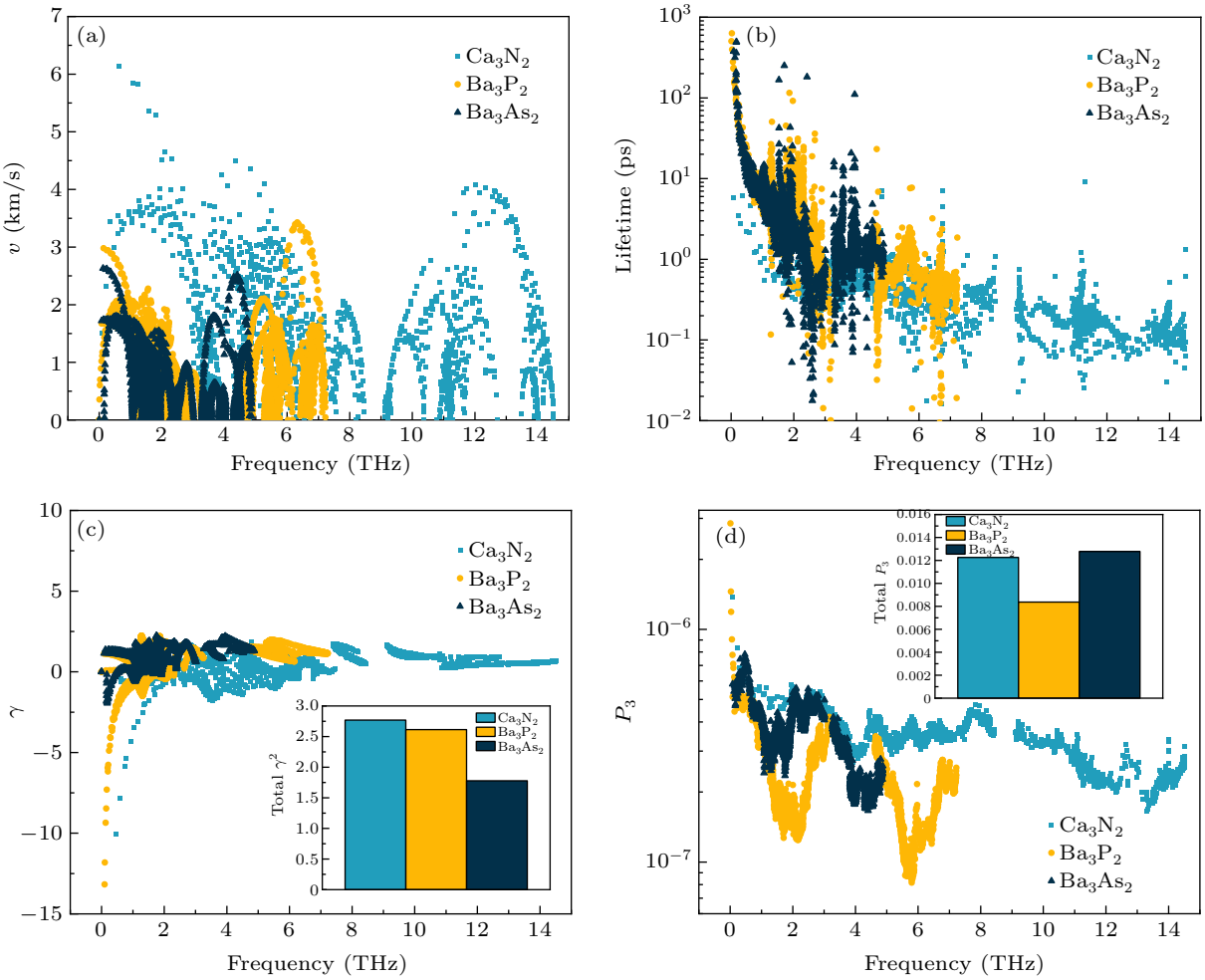



**Fig. 5.** Comparison of phonon modes, including (a) group velocity ($v$), (b) phonon lifetime ($\tau$), (c) Grüneisen parameter ($\gamma$) and total $\gamma^2$, (d) three-phonon scattering phase space ($P_3$) and total $P_3$, for $Ca_3N_2$, $Ba_3P_2$, and $Ba_3As_2$.

In order to further reveal the thermal transport properties in such 2D materials, phonon mode information, including phonon group velocity ($v$) and lifetime ($\tau$), are systematically investigated, and the results are plotted in Fig. 5. It is well known that the phonon group velocity, defined as the gradient of the phonon dispersion relation ($v = \partial\omega_q/\partial q$), governs the propagation of vibrational energy. It can be observed from Fig. 5(a) that although the $Ca_3N_2$ hosts higher group velocities than $Ba_3P_2$ and $Ba_3As_2$ in almost all frequency regions, its $\kappa_L$ is the lowest at 300 K (6.12 W/mK) among the three 2D materials. This paradox could be resolved by analyzing the phonon lifetimes, which are inversely proportional to phonon scattering rates. As shown in Fig. 5(b), compared to $Ba_3P_2$ and $Ba_3As_2$, the $Ca_3N_2$ exhibits markedly shorter $\tau$ at the low-frequency region. It should be noted here that the influence of high frequency phonon lifetime on thermal conductivity becomes statistically significant primarily at elevated temperatures. That is to say, the lower thermal conductivity of $Ca_3N_2$ mainly originates from the shorter phonon lifetime in the low-frequency region. The phonon lifetime is mainly determined by the phonon anharmonicity (scattering intensity) and scattering phase space (scattering probability). The scattering intensity could be reflected by the Grüneisen parameter.[39,40] From Fig. 5(c), it can be noted that the $Ca_3N_2$ possesses a larger $\gamma^2$, and a larger $\gamma^2$ represents stronger scattering intensity and lower thermal conductivity. For the scattering phase space, which is determined by energy and momentum conservation rules, it also governs thermal resistance. As shown in Fig. 5(d), $Ca_3N_2$ and $Ba_3As_2$ exhibit a significantly larger three-phonon scattering phase space com-

pared to $Ba_3P_2$, which means that $Ca_3N_2$ and $Ba_3As_2$ have a greater possibility of anharmonic phonon scattering. The root mean square displacement (RMSD) determines the distance of atoms from the equilibrium position and the sensitivity to the potential energy surface, which quantifies the anharmonic effects.[41–43] As shown in Fig. 6, one can note that $Ca_3N_2$ exhibits a larger RMSD value, implying stronger anharmonicity. Consequently, the low thermal conductivity of $Ca_3N_2$ is predominantly attributed to the larger Grüneisen parameter and scattering phase space. At lower temperatures, $Ca_3N_2$ (51.9 W/mK at 50 K) exhibits lower thermal conductivity than $Ba_3P_2$ (82.2 W/mK at 50 K) and $Ba_3As_2$ (60.1 W/mK at 50 K). As temperature increases, however, an opposite trend emerges, where the thermal conductivity of $Ca_3N_2$, $Ba_3P_2$, and $Ba_3As_2$ are 2.1 W/mK, 2.9 W/mK, and 1.9 W/mK at 800 K, respectively. This phenomenon is attributed to the synergistic effect of larger phonon lifetimes and higher group velocities in the high-frequency region, which result in a slower decline of thermal conductivity with temperature for $Ca_3N_2$, compared to $Ba_3P_2$ and $Ba_3As_2$.

The discussion on anharmonicity should not be limited to three-phonon scattering.[44] Four-phonon scattering also plays a critical role in certain materials.[45,46] Our study reveals that four-phonon interactions exert the most significant influence on $Ba_3As_2$, as evidenced by its largest total $P_4$ value shown in Table 1. Notably, previous research has employed the $P_4/P_3$ ratio as a criterion to assess the impact of four-phonon effects, assuming that four-phonon effects are negligible when $P_4 < P_3$. As shown in Fig. 7, the $P_4/P_3$ ratio of $Ba_3P_2$ is significantly higher than that of $Ba_3As_2$. This behavior can be observed more intuitively in Fig. 7(d). In this case, the four-phonon scattering in $Ba_3P_2$ should exhibit a stronger suppression effect on lattice thermal conductivity than that in $Ba_3As_2$. However, contrary to expectations, when four-phonon scattering is considered, the suppression rate of thermal conductivity in $Ba_3P_2$ is actually smaller than in $Ba_3As_2$. That is to say, the suppression of thermal conductivity by four-phonon scattering cannot be evaluated solely from the ratio of $P_4/P_3$.

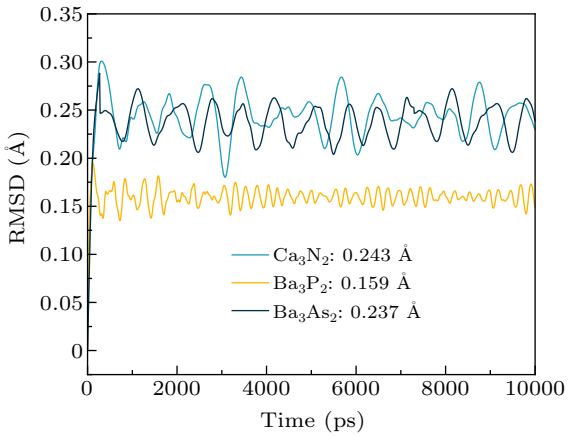



**Fig. 6.** RMSD of $Ca_3N_2$, $Ba_3P_2$, and $Ba_3As_2$ as a function of time.

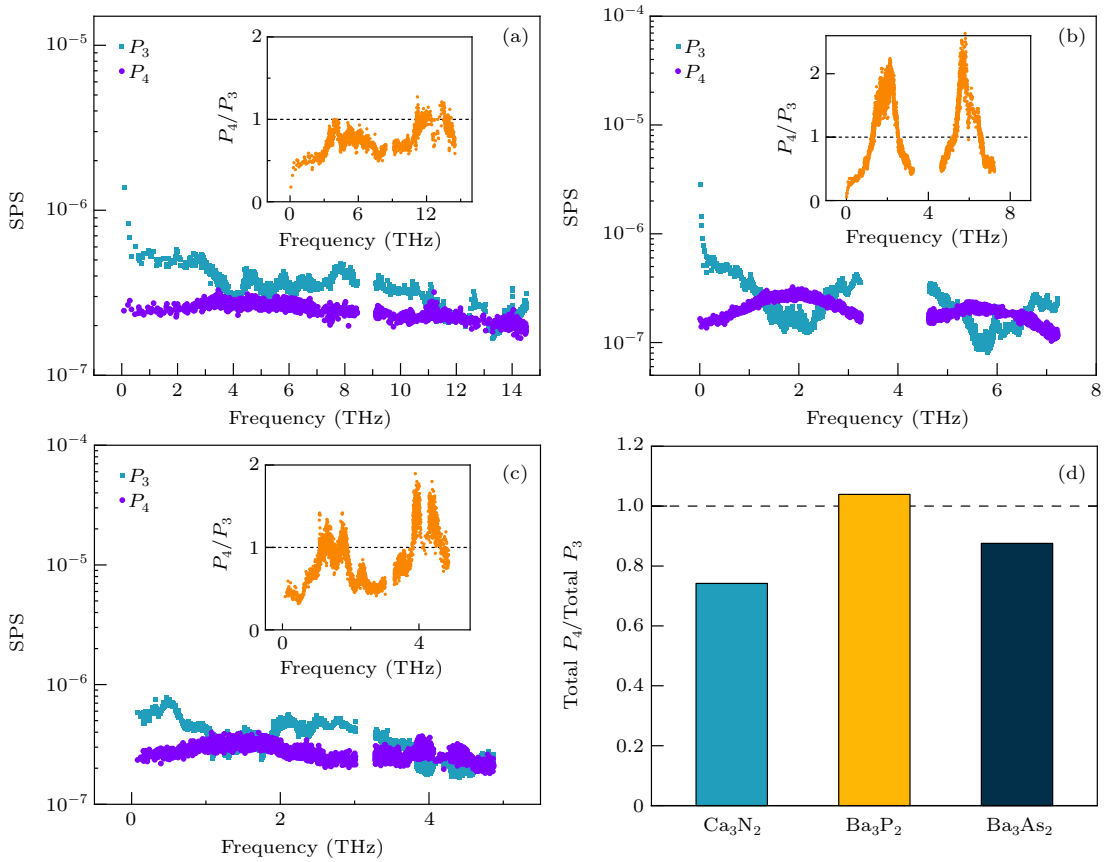



**Fig. 7.** Comparison of 3ph and 4ph scattering phase spaces (SPS) for (a) $Ca_3N_2$, (b) $Ba_3P_2$, and (c) $Ba_3As_2$. (d) Total $P_4$/total $P_3$ of $Ca_3N_2$, $Ba_3P_2$, and $Ba_3As_2$.

## 4. Conclusion

In this work, we investigated the thermal transport properties of 2D narrow-bandgap semiconductors ($Ca_3N_2$, $Ba_3P_2$, and $Ba_3As_2$) by combining the NEP with phonon Boltzmann transport theory. All three materials exhibit intrinsically low lattice thermal conductivity ($\kappa_L$). Specifically, the $\kappa_{3ph}$ values of $Ca_3N_2$, $Ba_3P_2$, and $Ba_3As_2$ are 6.60 W/mK, 11.90 W/mK, and 8.88 W/mK, respectively, which are further reduced to 6.12 W/mK, 9.73 W/mK, and 6.77 W/mK when four-phonon (4ph) scattering is included. Among them, $Ba_3As_2$ exhibits the strongest 4ph suppression effect (23.8% reduction), mainly attributed to its larger scattering phase space that facilitates stronger four-phonon interactions. In contrast, the low $\kappa_L$ of $Ca_3N_2$ originates from the combined effects of pronounced anharmonicity and short phonon lifetimes.

Previous studies commonly estimated the impact of four-phonon scattering on thermal conductivity by comparing the ratio of $P_4$ to $P_3$ scattering phase spaces. However, our results reveal that although $Ba_3P_2$ has a higher $P_4/P_3$ ratio than $Ba_3As_2$, its four-phonon scattering produces a weaker suppression effect on thermal conductivity. This finding demonstrates that relying solely on the $P_4/P_3$ ratio is insufficient to evaluate the strength of four-phonon scattering. Overall, this work provides new insights into the thermal transport behavior of emerging 2D narrow-bandgap semiconductors and offers a theoretical foundation for their future applications in thermal management and related technologies.

## Data availability statement

The data that support the findings of this study are openly available at https://github.com/wenlongli-567/data.

## Acknowledgments

This work was supported by the National Natural Science Foundation of China (Grant No. 52372260), the Science Fund for Distinguished Young Scholars of Hunan Province (Grant Nos. 2024JJ2048 and 2021JJ10036), the Science and Technology Innovation Program of Hunan Province (Grant No. 2022RC1197), and the Scientific Research Fund of Hunan Provincial Education Department (Grant No. 22B0512).

## References

[1] Geng J, Zhang P, Tang Z and Ouyang T 2024 *Chin. Phys. B* **33** 046501
[2] Lu J, Cui C, Ouyang T, Li J, He C, Tang C and Zhong J 2023 *Chin. Phys. B* **32** 048401
[3] Seol J H, Jo I, Moore A L, Lindsay L, Aitken Z H, Pettes M T, Li X, Yao Z, Huang R and Broido D 2010 *Science* **328** 213
[4] Li S, Qin Z, Wu H, Li M, Kunz M, Alatas A, Kavner A and Hu Y 2022 *Nature* **612** 459
[5] Wang Y, Xu N, Li D and Zhu J 2017 *Adv. Funct. Mater.* **27** 1604134
[6] Zhang G and Zhang Y W 2017 *Chin. Phys. B* **26** 034401
[7] Liu L, Feng Y and Shen Z 2003 *Phys. Rev. B* **68** 104102
[8] Roy S, Zhang X, Puthirath A B, Meiyazhagan A, Bhattacharyya S, Rahman M M, Babu G, Susarla S, Saju S K and Tran M K 2021 *Adv. Mater.* **33** 2101589
[9] Ling X, Wang H, Huang S, Xia F and Dresselhaus M S 2015 *Proc. Natl. Acad. Sci.* **112** 4523
[10] Li L, Yu Y, Ye G J, Ge Q, Ou X, Wu H, Feng D, Chen X H and Zhang Y 2014 *Nat. Nanotechnol.* **9** 372
[11] Manzeli S, Ovchinnikov D, Pasquier D, Yazyev O V and Kis A 2017 *Nat. Rev. Mater.* **2** 17033
[12] Wang Q H, Kalantar-Zadeh K, Kis A, Coleman J N and Strano M S 2012 *Nat. Nanotechnol.* **7** 699
[13] Chen Q Y, Huang F J, Ruan J Q, Zhao Y F, Zhang X F, Xiong K and He Y 2024 *Phys. Rev. Appl.* **22** 034013
[14] Behler J 2016 *J. Chem. Phys.* **145** 170901
[15] Schran C, Thiemann F L, Rowe P, Müller E A, Marsalek O and Michaelides A 2021 *Proc. Natl. Acad. Sci. USA* **118** e2110077118
[16] Bartók A P, Payne M C, Kondor R and Csányi G 2010 *Phys. Rev. Lett.* **104** 136403
[17] Bartók A P and Csányi G 2015 *Int. J. Quantum Chem.* **115** 1051
[18] Lysogorskiy Y, van der Oord C, Bochkarev A, Menon S, Rinaldi M, Hammerschmidt T, Mrovec M, Thompson A, Csányi G and Ortner C 2021 *npj Comput. Mater.* **7** 97
[19] Bochkarev A, Lysogorskiy Y, Ortner C, Csányi G and Drautz R 2022 *Phys. Rev. Res.* **4** L042019
[20] Wang H, Zhang L and Han J 2018 *Comput. Phys. Commun.* **228** 178
[21] Han J, Zhang L and Car R 2018 *Commun. Comput. Phys.* **23** 629
[22] Shapeev A V 2016 *Multiscale Model. Simul.* **14** 1153
[23] Novoselov I, Yanilkin A, Shapeev A and Podryabinkin E 2019 *Comput. Mater. Sci.* **164** 46
[24] Fan Z, Zeng Z, Zhang C, Wang Y, Song K, Dong H, Chen Y and Ala-Nissila T 2021 *Phys. Rev. B* **104** 104309
[25] Fan Z 2022 *J. Phys.: Condens. Matter* **34** 125902
[26] Fan Z, Wang Y, Ying P, Song K, Wang J, Wang Y, Zeng Z, Xu K, Lindgren E and Rahm J M 2022 *J. Chem. Phys.* **157** 114801
[27] Tang Z, Wang X, He C, Li J, Chen M, Tang C and Ouyang T 2024 *Phys. Rev. B* **110** 134320
[28] Zhang J, Zhang H C, Li W and Zhang G 2024 *Chin. Phys. B* **33** 047402
[29] Kresse G and Furthmüller J 1996 *Phys. Rev. B* **54** 11169
[30] Blöchl P E 1994 *Phys. Rev. B* **50** 17953
[31] Kresse G and Joubert D 1999 *Phys. Rev. B* **59** 1758
[32] Perdew J P, Burke K and Ernzerhof M 1996 *Phys. Rev. Lett.* **77** 3865
[33] Ziman J M 2001 *Electrons and Phonons: The Theory of Transport Phenomena in Solids* (Oxford: Oxford University Press)
[34] Zhou H, Zhou S, Hua Z, Bawane K and Feng T 2023 *Appl. Phys. Lett.* **123** 192201
[35] Togo A and Tanaka I 2015 *Scr. Mater.* **108** 1
[36] Li W, Carrete J, Katcho N A and Mingo N 2014 *Comput. Phys. Commun.* **185** 1747
[37] Han Z, Yang X, Li W, Feng T and Ruan X 2022 *Comput. Phys. Commun.* **270** 108179
[38] Guo Z, Han Z, Feng D, Lin G and Ruan X 2024 *npj Comput. Mater.* **10** 31
[39] Broido D, Lindsay L and Ward A 2012 *Phys. Rev. B* **86** 115203
[40] Tong Z, Dumitrica T and Frauenheim T 2021 *Nano Lett.* **21** 4351
[41] Parrish K D, Jain A, Larkin J M, Saidi W A and McGaughey A J 2014 *Phys. Rev. B* **90** 235201
[42] Cui C, Zhang Y, Ouyang T, Chen M, Tang C, Chen Q, He C, Li J and Zhong J 2023 *Phys. Rev. Mater.* **7** 033803
[43] Tang Z, Wang X, Li J, He C, Tang C, Wang H, Chen M and Ouyang T 2023 *Appl. Phys. Lett.* **122** 172203
[44] Sun J, Liu X, Xiong Y, Yao Y, Yang X, Shao C, Wang R and Li S 2025 *Appl. Phys. Lett.* **126** 112112
[45] Feng T, Lindsay L and Ruan X 2017 *Phys. Rev. B* **96** 161201
[46] Yang X, Feng T, Li J and Ruan X 2019 *Phys. Rev. B* **100** 245203